Supplementary Material

Molecular Reaction and Solvation Visualized by Time-Resolved X-ray Solution Scattering: Structure, Dynamics, and Their Solvent Dependence

Kyung Hwan Kim, Jeongho Kim, Jae Hyuk Lee, and Hyotcherl Ihee

Supplementary Methods

Polychromatic correction

The spectrum of X-ray pulses used in the experiment has a bandwidth of 3 % with a characteristic semi-Gaussian shape (Figure 5a). This polychromatic X-ray spectrum is convoluted with $\Delta S_{mono}(q)$ to give the measured data:

$$\Delta S(2\theta) = \frac{\int \Delta S_{mono}(q) P(\lambda) d\lambda}{\int P(\lambda) d\lambda}, \tag{S1}$$

where $\Delta S(2\theta)$ is the observed scattering signal as a function of the scattering angle (2θ), $\Delta S_{mono}(q)$ is the scattering signal from monochromatic X-rays, and $P(\lambda)$ is the X-ray spectrum (in Figure 5a). The polychromatic X-ray beam gives rise to a small shift and damping of $\Delta S(2\theta)$ in the high 2θ region. Consequently, its Fourier transform, $\Delta S(r)$, also changes compared to the one obtained by monochromatic X-rays. The effect of the polychromatic beam on $\Delta S(r)$ is demonstrated in Figure 5b. In order to get accurate distance information from the X-ray scattering data, it is necessary to correct for the effect of polychromaticity on $\Delta S(r)$. If the X-ray wavelength changes from λ_0 to λ' ($\lambda' = a\lambda_0$), the scattering intensity at the new wavelength, $\Delta S_{mono,\lambda'}(q')$, can be defined as $\Delta S_{mono,\lambda'}(q') = \Delta S_{mono,\lambda_0}(q)$, where $q' = q/a$. If $P(\lambda)$ is normalized, Eq. (5) is simplified to

$$\Delta S(2\theta) = \int \Delta S_{mono,\lambda}(q) P(\lambda) d\lambda . \tag{S2}$$

Eq. (6) can be converted to a discrete sum,

$$\Delta S(2\theta) = \sum_{\lambda} \Delta S_{mono,\lambda_i}(q) P(\lambda_i) . \tag{S3}$$

The Fourier transform of $\Delta S(q)$ is as follows (ignoring the constant term):

$$\begin{aligned} r\Delta S(r) &= \int_0^{q_{\max}} q\Delta S(q)\sin(qr)dq \\ &= \int_0^{q_{\max}} q\Delta S(2\theta)\sin(qr)dq \end{aligned} . \tag{S4}$$

Then, inserting Eq. (7) into Eq. (8) leads to

$$
\begin{aligned}
r\Delta S(r) &= \int_0^{q_{\max}} q\sin(qr)dq \sum P(\lambda_i)\Delta S_{mono,\lambda_i}(q) \\
&= \sum P(\lambda_i) \int_0^{q_{\max}} q\Delta S_{mono,\lambda_i}(q)\sin(qr)dq \,. \\
&= \sum r\Delta S_{mono,\lambda_i}[r]P(\lambda_i)
\end{aligned}
\tag{S5}
$$

This equation shows that the scattering data from polychromatic beam can be regarded as a weighted sum of monochromatic scattering data in real space.

Based on the relationship in *q*-space, $\Delta S_{mono,\lambda'}(q/a) = \Delta S_{mono,\lambda_0}(q)$, where *a* is the ratio between two wavelengths, the relationship in *r*-space between the data at the two wavelengths is defined as follows:

$$
\begin{aligned}
r\Delta S_{mono,\lambda_0}(r) &= \int_0^{q_{\max}} q\Delta S_{mono,\lambda_0}(q)\sin(qr)dq \\
&= \int_0^{q_{\max}} q\Delta S_{mono,\lambda'}(q/a)\sin(qr)dq \\
&= \int_0^{q_{\max}} a'q'\Delta S_{mono,\lambda'}(q')\sin(aq'r)adq' \\
&= a^2 \int_0^{q_{\max}} q'\Delta S_{mono,\lambda'}(q')\sin(q'ar)dq'
\end{aligned}
\,. \tag{S6}
$$

Substituting *ar* for *r′* gives a new Fourier transform equation for $\Delta S_{\mathrm{mono},\lambda'}(r')$:

$$
\begin{aligned}
r\Delta S_{mono,\lambda_0}(r) &= a^2 \int_0^{q_{\max}} q'\Delta S_{mono,\lambda'}(q')\sin(q'r')dq' \\
&= a^2 r'\Delta S_{mono,\lambda'}(r') \\
&= a^3 r\Delta S_{mono,\lambda'}(ar)
\end{aligned}
\,. \tag{S7}
$$

By swapping the left and right sides of and simplifying Eq. (11), the following equation is obtained:

$$
r\Delta S_{mono,\lambda'}(r) = \frac{1}{a^3} r\Delta S_{mono,\lambda_0}(r/a)\,. \tag{S8}
$$

Finally, inserting Eq. (12) into Eq. (9) yields

$$r\Delta S_{poly}(r) = \sum_{\lambda} r\Delta S(r)_{mono,\lambda_i} P(\lambda_i) = \sum_{\lambda} \frac{1}{a_i^3} r\Delta S_{mono,\lambda_0}(r/a_i) P(\lambda_i) \quad \text{(S9)}$$

Using Eq. (S9), $\Delta S(r)$ curve from a polychromatic X-ray beam can be easily constructed by a linear combination of $\Delta S(r)$'s obtained by monochromatic X-ray beams at many different X-ray wavelengths. Conversely, $\Delta S(r)$ in monochromatic condition can be extracted from the polychromatic data by least-squares fitting. As shown in Figure 5b, we can start with a trial scattering curve and convolute it with the polychromatic spectrum. By comparison between polychromatic experimental data and the trial curve convoluted with the polychromatic X-ray spectrum, $\Delta S(r)$ under monochromatic condition can be extracted by least-squares refinement. The polychromatic experimental $\Delta S(r)$ was used as the initial trial data. In practice, the trial data is divided into 50 intervals along r-axis with a 5^{th}-order polynomial representing each interval. These intervals are connected smoothly using b-spline smoothing. The polychromatic correction is applied to this trial data, and the least-squares refinement in comparison with the polychromatic experimental data gives $\Delta S(r)$ under monochromatic condition, which can be used for further data analysis. The monochromatic $\Delta S(r,t)$'s were obtained using this protocol and the results are shown in Figure S1.

Experimental data, $r^2\Delta S(r)$, and radial distribution function, $\rho(r)$

The static scattering intensity is calculated from the atom–atom pair distribution function $g_{ij}(r)$ as follows:

$$S(q) = \sum_i N_i f_i^2(q) + \sum_i \sum_{i \neq j} \frac{N_i N_j}{V} f_i(q) f_j(q) \int_0^{\infty} (g_{ij}(r) - 1) \frac{\sin(qr)}{qr} 4\pi r^2 dr . \quad \text{(S10)}$$

The first term in Eq. (S10) is not included in the difference scattering because it does not depend on the molecular structure. Then, the difference scattering intensity, $\Delta S(q)$, is described in terms of difference pair distribution function, $\Delta g_{ij}(r)$, as follows:

$$\Delta S(q) = \sum_i \sum_{i \neq j} \frac{N_i N_j}{V} f_i(q) f_j(q) \int_0^{\infty} \Delta g_{ij}(r) \frac{\sin(qr)}{qr} 4\pi r^2 dr . \quad \text{(S11)}$$

For an I_2 molecule, Eq. (15) can be written as

$$\Delta S(q) = \frac{N_{I_1} N_{I_2}}{V} f_I{}^2(q) \int_0^\infty \Delta g_{I_1 I_2}(r) \frac{\sin(qr)}{q} 4\pi r dr$$

$$q\Delta S(q) = 4\pi \frac{N_{I_1} N_{I_2}}{V} f_I{}^2(q) \int_0^\infty r \Delta g_{I_1 I_2}(r) \sin(qr) dr \ . \quad \text{(S12)}$$

$$\frac{q\Delta S(q)}{f_I{}^2(q)} = 4\pi \frac{N_{I_1} N_{I_2}}{V} \int_0^\infty r \Delta g_{I_1 I_2}(r) \sin(qr) dr$$

In Eq. (S12), f_I is the scattering factor of iodine atom and sharpens the peaks resulting from sine-Fourier transform (sharpening term). The sine-Fourier transform of $\frac{q\Delta S(q)}{f_I{}^2(q)}$ is

$$\frac{1}{2\pi^2 r} \int_0^\infty \frac{q\Delta S(q)}{f_I{}^2(q)} \sin(qr) dq = \frac{N_{I_1} N_{I_2}}{V} \Delta g_{I_1 I_2}(r) . \quad \text{(S13)}$$

In Eq. (3), the damping term, $\exp(-q^2\alpha)$, can be replaced by $\int_{-\infty}^{\infty} \sqrt{\frac{\pi}{\alpha}} \exp\left(-\frac{r'^2}{4\alpha}\right) \exp(iqr') dr'$ and then replacing the integrand in Eq. (3) by Eq. (S13) leads to the following relations:

$$\begin{aligned}
\Delta S[r] &= \frac{1}{2\pi^2 r} \int_0^\infty \frac{q\Delta S(q)}{f_I{}^2(q)} \exp(-q^2\alpha) \sin(qr) dq \\
&= \frac{1}{2\pi^2 r} \int_0^\infty \frac{q\Delta S(q)}{f_I{}^2(q)} \int_{-\infty}^\infty \sqrt{\frac{\pi}{\alpha}} \exp\left(-\frac{r'^2}{4\alpha}\right) \exp(iqr') dr' \sin(qr) dq \\
&= \frac{1}{4\pi^2 r} \int_{-\infty}^\infty \frac{q\Delta S(q)}{f_I{}^2(q)} \int_{-\infty}^\infty \sqrt{\frac{\pi}{\alpha}} \exp\left(-\frac{r'^2}{4\alpha}\right) \exp(iqr') dr' \exp(-iqr) dq \\
&= \frac{1}{4\pi^2 r} \sqrt{\frac{\pi}{\alpha}} \int_{-\infty}^\infty \exp\left(-\frac{r'^2}{4\alpha}\right) \int_{-\infty}^\infty \frac{q\Delta S(q)}{f_I{}^2(q)} \exp(-iq(r-r')) dq dr' \\
&= \frac{1}{2} \sqrt{\frac{\pi}{\alpha}} \int_{-\infty}^\infty \exp\left(-\frac{r'^2}{4\alpha}\right) \frac{N_{I_1} N_{I_2}}{V} \Delta g_{I_1 I_2}(r-r') dr' \\
&= \frac{1}{2} \sqrt{\frac{\pi}{\alpha}} \frac{N_{I_1} N_{I_2}}{V} \int_{-\infty}^\infty \exp\left(-\frac{r'^2}{4\alpha}\right) \Delta g_{I_1 I_2}(r-r') dr' \\
\Delta S[r] &= \sqrt{\frac{\pi}{\alpha}} \frac{N_{I_1} N_{I_2}}{2V} \Delta g_{I_1 I_2}(r) * \exp\left(-\frac{r^2}{4\alpha}\right) \quad . \quad \text{(S14)}
\end{aligned}$$

where the asterisk (*) stands for convolution and the sharpening constant of α = 0.03 Å^2 was used for I_2.

By multiplying r^2 to both sides of the last equation in Eq. (14), the relationship between $r^2\Delta S(r)$ and $\Delta\rho(r)$ for an I_2 molecule can be obtained:

$$\begin{aligned} r^2\Delta S(r) &= \sqrt{\frac{\pi}{\alpha}}\frac{N_{I_1}N_{I_2}}{2V} r^2\Delta g_{I_1I_2}(r) * \exp(-r^2/4\alpha) \\ &= \sqrt{\frac{\pi}{\alpha}}\frac{N_{I_1}N_{I_2}}{2V} \Delta\rho(r) * \exp(-r^2/4\alpha) \\ r^2 S(r) &= r^2\Delta S(r) + \sqrt{\frac{\pi}{\alpha}}\frac{N_{I_1}N_{I_2}}{2V} \rho_0(r) * \exp(-r^2/4\alpha). \\ &= \sqrt{\frac{\pi}{\alpha}}\frac{N_{I_1}N_{I_2}}{2V} \left(\Delta\rho(r) + \rho_0(r)\right) * \exp(-r^2/4\alpha) \\ &= \sqrt{\frac{\pi}{\alpha}}\frac{N_{I_1}N_{I_2}}{2V} \rho(r) * \exp(-r^2/4\alpha) \end{aligned} \quad \text{(S15)}$$

Retrieving $r^2\Delta S_{inst}(r,t)$ by deconvolution

The procedure of deconvolution is as follows. Because the experimental data is convoluted with the X-ray pulse profile in time, the least-mean-squares algorithm was applied to the experimental data $r^2\Delta S(r,t)$ for each r independently. For a given r_i, a model function for $r_i^2\Delta S_{inst}(r_i,t)$ was considered as a sum of three exponentials. Coefficients and time constants of the exponentials were used as fitting parameters of the least-squares fitting that optimizes $r_i^2\Delta S_{inst}(r_i,t)$ for each r_i by minimizing the discrepancy between the experimental $r_i^2\Delta S(r,t)$ and the model function $r_i^2\Delta S_{inst}(r_i,t)$ convoluted with the X-ray temporal profile. The X-ray pulse profile, $I_{x\text{-}ray}(t)$, shown in Figure 6a was approximated by four half-Gaussians that give a perfect fit to the X-ray temporal profile measured by a streak camera. Note that the rising edge of the X-ray pulse (negative time) is slightly steeper that the falling edge in Figure 6a. The quality of the deconvolution were checked by convoluting $r^2\Delta S_{inst}(r,t)$ with $I_{x\text{-}ray}(t)$ and then comparing it with $r^2\Delta S(r,t)$. The deconvoluted $r^2\Delta S_{inst}(r,t)$ curves gave good agreement for both I_2 in CCl_4 and I_2 in cyclohexane.

Molecular dynamics simulation

All the molecular dynamics (MD) simulations were performed with periodic boundary conditions for a cubic box of 43.6 Å length consisting of one I_2 molecule embedded in 511 CCl_4 molecules. This setup corresponded to the density of CCl_4 at standard temperature and pressure (1.58 g/cm^3). The classical equations of motion were integrated using the Gear predictor-corrector method with a time step of 1 fs, and the solvent molecules were kept rigid using quaternions. Freezing the vibrational degrees of freedom of CCl_4 was in agreement with previous studies, which favoured the V-T energy transfer during the vibrational relaxation of I_2.

All interactions were assumed to be pairwise additive; for the intermolecular C-C, Cl-Cl, and C-Cl interactions, the OPLS parameters for Lennard-Jones 6-12 and Coulomb potentials were used. The I-C and I-Cl interactions were modeled by Lennard-Jones 6-12 potentials with parameters constructed using the usual Lorentz-Berthelot mixing rules, where ε_I = 240 K and σ_I = 3.8 Å were determined from a fit of parameters for I-Ne and I-Ar interactions. The cutoff distance for terminating the van der Waals dispersion forces was set to be half of the box length. The electronic ground state (X state) of I_2 was represented by a Morse potential V_X with the parameters D_e = 12547 cm^{-1}, β = 1.91 Å^{-1}, and r_{eq} = 2.67 Å. The purely repulsive excited state (Π state) was of the form $V_\Pi(r) = \alpha\,(r/\text{Å})^{-9.5}$ with $\alpha = 8.61\times10^7$ cm^{-1}, and its dissociation limit was identical to that of the *X*-state.

The initial conditions for the photodissociation calculations were found by MD simulations performed in the canonical ensemble at T = 300 K using the Nose-Hoover thermostat. For these equilibration runs, the initial center-of-mass coordinates of the molecules corresponded to the positions of the unit cells in the cubic simulation box, and the momentum components of each atom were chosen randomly from a distribution with a Gaussian weighting. This choice did not bias the ensemble sampling because position randomization was obtained from a 20-ps initial run, before all atomic positions and velocities were saved for every 10 ps (each set of atomic positions and velocities constituted the initial conditions for the photodissociation calculations). The I_2 molecule was kept rigid during the equilibration runs with a separation equal to the classical equilibrium distance r_{eq}.

The photodissociation trajectories were performed in the microcanonical ensemble to avoid non-collisional velocity scaling from the Nose-Hoover thermostat. A total of 272 initial

conditions were used to run 200-ps photodissociation trajectories, where an instantaneous replacement of the X state by the Π state potential mimicked an optical laser excitation of I_2 from the X state to the Π state. Hence, at the first integration step, the total energy of the system increased by ~ 20000 cm^{-1} (the energy difference between the two electronic states at the distance r_{eq}, see Fig. 1). In 32 trajectories the iodine atoms escaped the solvent cage and did not recombine within 200 ps. This corresponds to approximately 12 %, which match previous experimental results.

Supplementary Figure

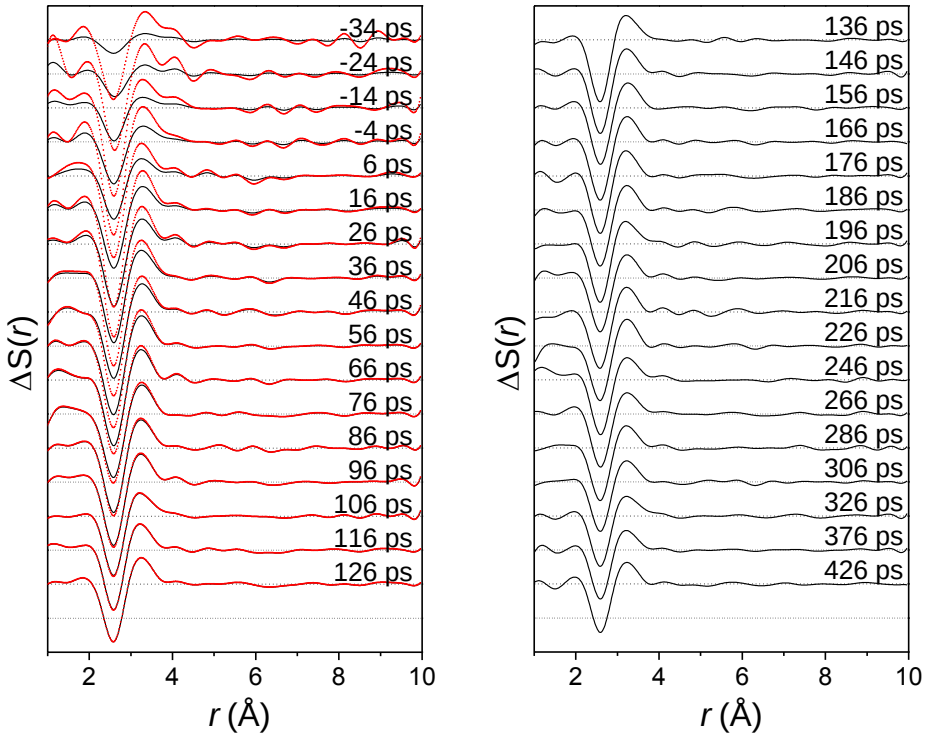

Figure S1. Polychromaticity-corrected $\Delta S(r,t)$ curves for I_2 in CCl_4. In the red dotted curves, the partial overlap of the laser illumination and X-ray pulse at early times was corrected by normalizing the curves with respect to the number of X-ray photons influenced by laser illumination.